Available online at www.sciencedirect.com

SCIENCE DIRECT®

Journal of Nuclear Materials 327 (2004) 188–193

journal of nuclear materials

www.elsevier.com/locate/jnucmat

Neutron tomographic investigations of boron-alloyed steels

M. Zawisky [a,*], M. Bastürk [a], J. Rehacek [b], Z. Hradil [b]

[a] *Atominstitute of the Austrian Universities, Stadionallee 2, A-1020 Vienna, Austria*
[b] *Department of Optics, Palacky University, 17. listopadu 50, CZ-77200 Olomouc, Czech Republic*

Received 7 January 2004; accepted 9 February 2004

Abstract

Boron-alloyed steel sheets are used in nuclear engineering as neutron shielding for radioactive waste disposal equipment. The ^{10}B isotope is a strong absorber of thermal neutrons but the transmission is enhanced by beam hardening of the polyenergetic neutrons in boron-alloyed steels. Therefore an algorithm for the correction of beam hardening was applied to the tomographic reconstruction of strong absorbing steel rods. We present tomographic studies on ^{10}B enriched steels and compare different reconstruction techniques, the filtered backprojection with and without beam hardening correction, and the maximum-likelihood method.

1. Introduction

This article is a continuation of our steel project [1], the quantitative analysis and 3D visualization of the ^{10}B isotope distribution in boron alloyed steels. This steel is used in nuclear engineering as neutron shielding for radioactive waste disposal equipment, such as components for compact fuel storage racks and transportation baskets [2]. The neutron attenuation in the steel depends mainly on the neutron energies and the uniform distribution of the ^{10}B isotope, which has a large attenuation cross-section for thermal neutrons ($\sigma_{\text{th}} = 3838.1(10)$ barn) [3]. The ^{10}B enrichment of the steels is rather expensive, therefore it is necessary for the steel manufacturer to exclude any systematic inhomogeneities. On the other hand, it is important for the customers to know how the effective cross-sections behave in polyenergetic neutron fields. Neutron transmission tomography (NT) is a sensitive technique for such investigations and we will show how the tomographic reconstruction can be adapted to the industrial demand. The steel inspections can also be performed on small reactor sources like the 250 kW TRIGA reactor at the Vienna Atominstitute, where a well-thermalized beam line is available for neutron radiography and tomography.

2. Correction of beam hardening

The use of polyenergetic neutron beams allows the investigation of thick steel sheets up to 2 cm, while the analysis with monochromatic neutrons is restricted to only a few millimeters at our institute [1]. The transmission analysis with thermal neutrons is of particular interest because it yields a realistic shielding factor of the steels, e.g., for the compact fuel storage in water. The transmission depends on the wavelength λ (thermal mean wavelength $\lambda_{\text{th}} = 0.18$ nm) and the distribution of the total thermal macroscopic cross-section ($\Sigma_{t,\text{th}}$) along the beam rays:

$$T(\lambda) \simeq \exp\left(-\frac{\lambda}{\lambda_{\text{th}}}\int_{\text{ray}} \Sigma_{t,\text{th}}(x,y,z)\,\mathrm{d}s\right). \tag{1}$$

Eq. (1) presumes a reciprocal velocity dependence of the involved cross-sections. This condition is fulfilled for the ^{10}B isotope and the boron-alloyed steel. The spectral change of the neutron flux in the sample, where preferably low energy neutrons with larger wavelengths are

---

[*] Corresponding author. Tel.: +43-1 58801 14170; fax: +43-1 58801 14199.

E-mail address: zawisky@ati.ac.at (M. Zawisky).

0022-3115/$ - see front matter © 2004 Elsevier B.V. All rights reserved.
doi:10.1016/j.jnucmat.2004.02.011

absorbed so that the remaining beam becomes richer in high energy (shorter wavelengths) neutrons, is called beam hardening. Beam hardening causes an elevation of the effective transmission T_{eff} in strong absorbing materials [4,5]. If the incoming neutron spectrum can be approximated by a Gaussian with mean wavelength $\bar{\lambda}$ then it has been verified [1] that the beam hardening effect can be corrected by an exponential correction term:

$$T_{\mathrm{eff}} \simeq \exp\left(-\frac{\bar{\lambda}}{\lambda_{\mathrm{th}}}\int_{\mathrm{ray}} \Sigma_{t,\mathrm{th}}(x,y,z)\,\mathrm{d}s\right) \times \exp\left(-\frac{\delta\lambda}{2\lambda_{\mathrm{th}}}\int_{\mathrm{ray}} \Sigma_{t,\mathrm{th}}(x,y,z)\,\mathrm{d}s\right)^{2}. \tag{2}$$

The beam hardening correction depends on the Gaussian width $\delta\lambda$, and on the samples composition and geometry. Fig. 1 shows the tomographic investigation of a ^{10}B enriched steel rod. The uncorrected reconstruction (left) reveals a strong apparent inhomogeneity in the macroscopic cross-sections due to the beam hardening effect. The corrected reconstruction (right) yields a rather homogeneous line profile, well in agreement with the uniform ^{10}B distribution in the sample, which was independently verified by neutron radiography and chemical analysis.

3. Comparison of different reconstruction techniques

3.1. Filtered backprojection

The filtered backprojection (FB) is a deterministic Fourier technique, which is widely used in CT imaging [4–6]. To reduce the low pass artifacts in discrete Fourier transformation we applied a Shepp–Logan filter [7] to all FB reconstructions. In the NT experiments we used a ^{6}LiF-ZnS(Ag) scintillation detector of 0.4 mm thickness, therefore one can assume a uniform detection probability within the range of thermal neutrons. Then the detector integrates Eq. (1) over the thermal wavelengths with the effective transmission T_{eff} as result. The tomographic reconstruction yields the spatial variation of the total effective cross-section along the beam rays:

$$\int_{\mathrm{ray}} \Sigma_{t,\mathrm{eff}}\,\mathrm{d}s \equiv -(\ln T_{\mathrm{eff}}). \tag{3}$$

According to Eq. (2) the effective transmission is enhanced in strong absorbing materials due to beam hardening. The enhancement of T_{eff} causes a reduction of $\Sigma_{t,\mathrm{eff}}$ towards the center of the rods (Fig. 1, left). Nevertheless, the analysis of effective cross-sections can be valuable for the manufacturer and customers as well, because it reveals how the steels act in a polyenergetic neutron field.

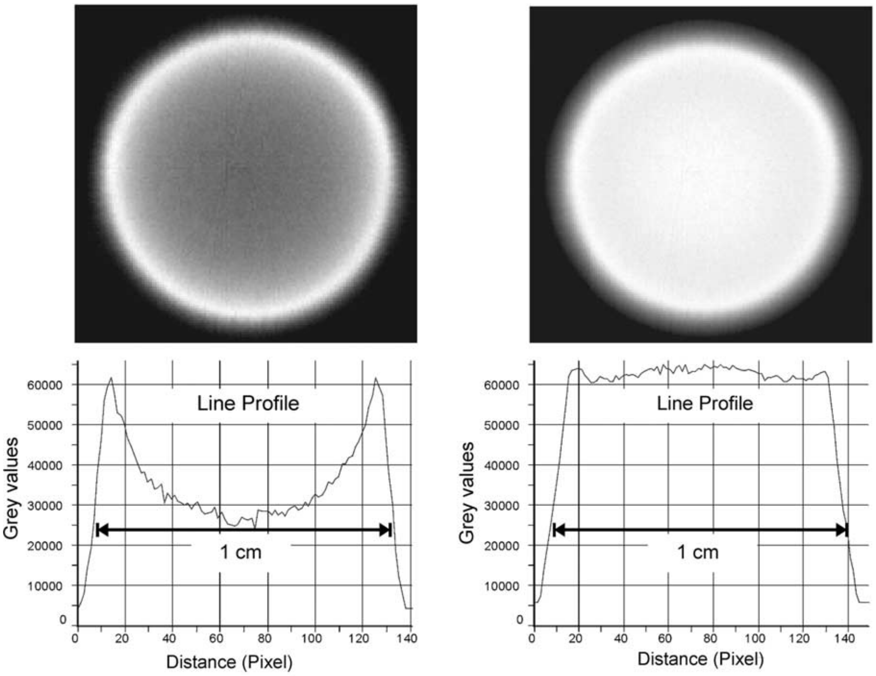

Fig. 1. Tomographic analysis of a ^{10}B enriched ($\Sigma_{t,\mathrm{th}} = 12.7$ cm^{-1}) steel rod of 1 cm diameter. Bright regions mark large macroscopic cross-sections. Left: the strong nonlinearity in the line profile through the sample is caused by the beam hardening effect. Right: after the beam hardening correction the homogeneity in the distribution of the total macroscopic cross-section has highly improved.

3.2. Filtered backprojection with beam hardening correction

Eq. (2) enables an approximate separation of the beam hardening effect from possible material inhomogeneities. To reconstruct highly inhomogeneous objects or objects whose compositions are totally unknown, more sophisticated measurements and analyses are needed. The inspection of Eq. (2) shows two basic generalizations of our tomographic investigations. If two sources of different mean wavelengths but same spectral widths are available, the subtraction of the corresponding signals yields,

$$\ln T_{\mathrm{eff}}(\lambda_1) - \ln T_{\mathrm{eff}}(\lambda_2) = -\frac{\bar{\lambda}_1 - \bar{\lambda}_2}{\lambda_{\mathrm{th}}} \int_{\mathrm{ray}} \Sigma_{t,\mathrm{th}}(x,y,z)\,\mathrm{d}s, \tag{4}$$

which is equivalent to the signal that would have been obtained with the monochromatic source of the effective wavelength $\lambda_{\mathrm{eff}} = \bar{\lambda}_1 - \bar{\lambda}_2$. Notice that these data analysis remove the beam hardening effect keeping the possibility to use standard fast FB routine for reconstruction.

Similarly, using two sources of the same central wavelength but of different spectral widths $\delta\lambda_1 > \delta\lambda_2$ we get,

$$-\sqrt{\ln T_{\mathrm{eff}}(\delta\lambda_1) - \ln T_{\mathrm{eff}}(\delta\lambda_2)} = -\frac{\sqrt{\delta\lambda_1^2 - \delta\lambda_2^2}}{2\lambda_{\mathrm{th}}} \int_{\mathrm{ray}} \Sigma_{t,\mathrm{th}}(x,y,z)\,\mathrm{d}s. \tag{5}$$

Such signal can be again interpreted as being a monochromatic radiation of the wavelength $\lambda_{\mathrm{eff}} = \sqrt{\delta\lambda_1^2 - \delta\lambda_1^2}/2$ transmitted through the sample.

In cases where the spectral characteristics $(\bar{\lambda}, \delta\lambda)$ are fixed without the possibility of modifying them there remains still the possibility to use an adaptive strategy, where the standard FB reconstruction is used for calculating the correction factor in Eq. (2). Corrected data then yield new better FB reconstruction and this procedure can be repeated until one gets a satisfactory fit of the experimental observations. In our investigations the correction was performed before the evaluation of the sinogram. This procedure yields the variation of the total thermal macroscopic cross-section, normalized to the mean wavelength $\bar{\lambda}$, as result. Such a corrected reconstruction facilitates the analysis of absorber homogeneity and density variations, and it is easy to achieve for simple geometrical objects (Fig. 1, right).

3.3. Maximum-likelihood reconstruction

The maximum-likelihood (ML) estimation is a powerful alternative to the standard FB technique. It provides significantly better results in the extreme cases of low count numbers, strong statistical fluctuations, and when only few projections are available or some projections are missing [8,9]. Basis of the ML reconstruction is the likelihood function (L), which combines the detection probabilities of all beam rays (b). The Poissonian fluctuation of the count numbers N_b in the detector pixels is correctly implemented in our ML routine:

$$L = \prod_b \frac{\overline{N}_b^{N_b} \mathrm{e}^{-\overline{N}_b}}{N_b!} \to \max. \tag{6}$$

Considering the sample as being comprised of small elementary homogeneous cells Σ_i, the likelihood is maximized by the iterative algorithm,

$$\Sigma_i^{(n+1)} = \Sigma_i^n \left(\frac{A_i}{B_i}\right)^q, \tag{7}$$

where

$$A_i = \sum_b c_{ib} N_b \frac{\overline{N}'_b}{\overline{N}'_b + \overline{D}_b}, \tag{8}$$

$$B_i = \sum_b c_{ib} (\overline{N}'_b + \overline{D}_b). \tag{9}$$

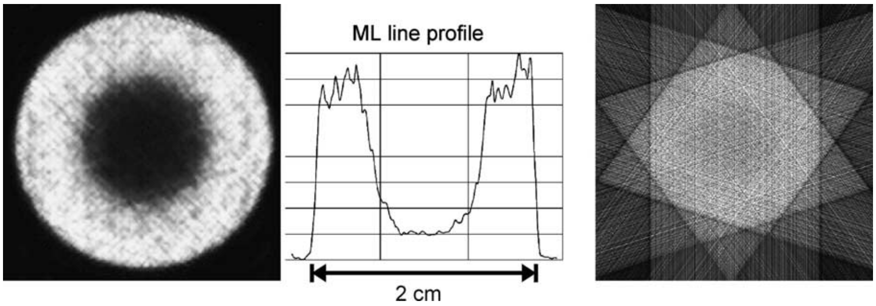

Fig. 2. Tomographic reconstructions of a boron alloyed steel ring ($\Sigma_{t,\mathrm{th}} = 4.4$ cm^{-1}) with 2 (1) cm diameter outside (inside). The reconstructions (left: maximum-likelihood, right: filtered backprojection) are achieved with only 10 projections.

c_{ib} being the overlap of bth observation and ith cell, and $\overline{D}_b$ being the estimated mean number of dark (background) counts, $\overline{N}_b = \overline{N}'_b + \overline{D}_b = \overline{N}_0 T_{\text{eff},b} + \overline{D}_b$, where $\overline{N}_0$ is the mean input intensity per pixel. The parameter q governs the convergence rate.

Fig. 2 shows a comparison of the ML and FB reconstruction in the extreme case of only 10 projections but without beam hardening correction. Optimal treatment of noisy measurements is an important feature of the maximum-likelihood technique. This is especially important for the investigation of strongly absorbing materials, where by definition, the counting numbers are very small. Let us note that the ML algorithm could also be adapted for the correction of the beam hardening effect (not presented here).

4. Tomographic investigations of ^{10}B enriched steel rods

The production of ^{10}B enriched steels is rather expensive, therefore all possible sources of systematic inhomogeneities during the production process (melting, welding, milling, cutting) must be excluded from a complete three-dimensional absorber analysis. Within the steel project, a set of boron alloyed steel rods with different ^{10}B enrichments was bored out of thick steel sheets at different locations. All tomographic measurements have been performed at the Vienna Atominstitute at a thermal beamline with a neutron flux of 1.4×10^5 $\text{s}^{-1}\,\text{cm}^{-2}$. The images are recorded with a nitrogen-cooled slow scan CCD camera after neutron-to-light conversion in the scintillator. The spatial resolution lies between 200 and 400 μm, depending on the sample–scintillator distance. The typical exposure time for one projection is 2 min and we chose about 60 projections for a strong absorbing rod. The total macroscopic cross-section is the sum of all isotope contributions, $\Sigma_t = \sum_i \Sigma_i = \Sigma_{\text{steel}} + \Sigma_{\text{boron}}$, with $\Sigma_{\text{steel}} = 1.25\ \text{cm}^{-1}$. Only the ^{10}B isotope contributes to Σ_{boron}. The macroscopic thermal cross-section relates to the density of the ^{10}B isotope in the steel:

$$\rho(^{10}\text{B}) = \frac{M(^{10}\text{B})\Sigma_{\text{th}}(^{10}\text{B})}{N_{\text{A}}\sigma_{\text{th}}(^{10}\text{B})}. \tag{10}$$

The atomic weight, $M(^{10}\text{B}) = 10.0129\ \text{g}\,\text{mol}^{-1}$, the Avogadro constant, $N_{\text{A}} = 6.02214199(47) \times 10^{23}\ \text{mol}^{-1}$, and the microscopic cross-section σ_{th} (^{10}B), are known with high accuracy. Eq. (5) is employed in quantitative transmission analysis for the determination of the material composition [1]. Only the variations of cross-sections are relevant in the tomographic investigation, but ratios of macroscopic cross-sections from different volume elements (voxels) are proportional to isotopic density ratios. If the composition in some part of the sample volume is known, then, according to Eq. (10), a quantitative tomographic analysis is possible.

Fig. 3 shows the reconstruction of the effective (left) and thermal (right) total cross-sections of a highly ^{10}B enriched steel rod. After the beam hardening correction a uniform distribution of the ^{10}B isotopes was confirmed in most of the steel rods, which is one of our main results

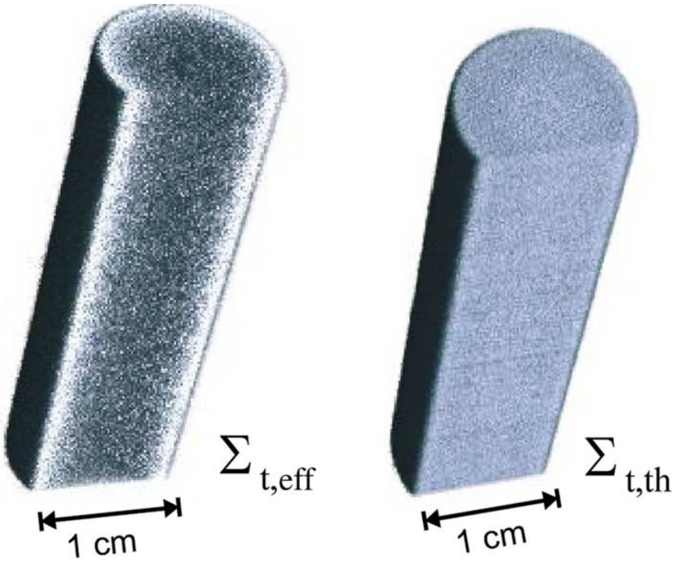

Fig. 3. 3D rendering of a highly enriched (^{10}B/B = 97.4 at.%) boron alloyed steel rod with 1 cm diameter ($\Sigma_{t,\text{th}} = 12.7\ \text{cm}^{-1}$). Left: variation of the effective total cross-sections. Right: beam hardening correction yields a uniform distribution of thermal cross-sections. Filtered backprojection from 60 projections, 2 min exposure time each.

of the tomographic investigations. When the absorption and the exponent in the correction term becomes too large then the beam hardening correction will fail. We found that the approximation of Eq. (2) is restricted to the regime $(d \cdot \Sigma_{t,\text{th}} \delta\lambda / 2\lambda_{\text{th}}) < 4$, where d is the maximum thickness of the sample.

The reconstruction of a two-component system is shown in Fig. 4. The inner rod with higher boron content is hardly resolved in the uncorrected FB reconstruction (Fig. 4, left), but it is clearly visible in the corrected image (Fig. 4, right). Certainly, the beam hardening correction is facilitated here by the known geometry of the steel composite. Note that the ratio of the line profiles (Fig. 4, middle-right) is in good agreement with the expected ratio of the cross-sections. The macroscopic cross-sections are derived from mass spectroscopic analysis plus density measurements of the two steel components. Our evaluations have been verified in radiographic neutron transmission experiments [1].

Fig. 5 demonstrates the advantages of the ML reconstruction. Although much less projections are considered here (only 10!), the result is better than the FB reconstruction in Fig. 4 (left). The good quality of the ML reconstruction is surprising because actually no

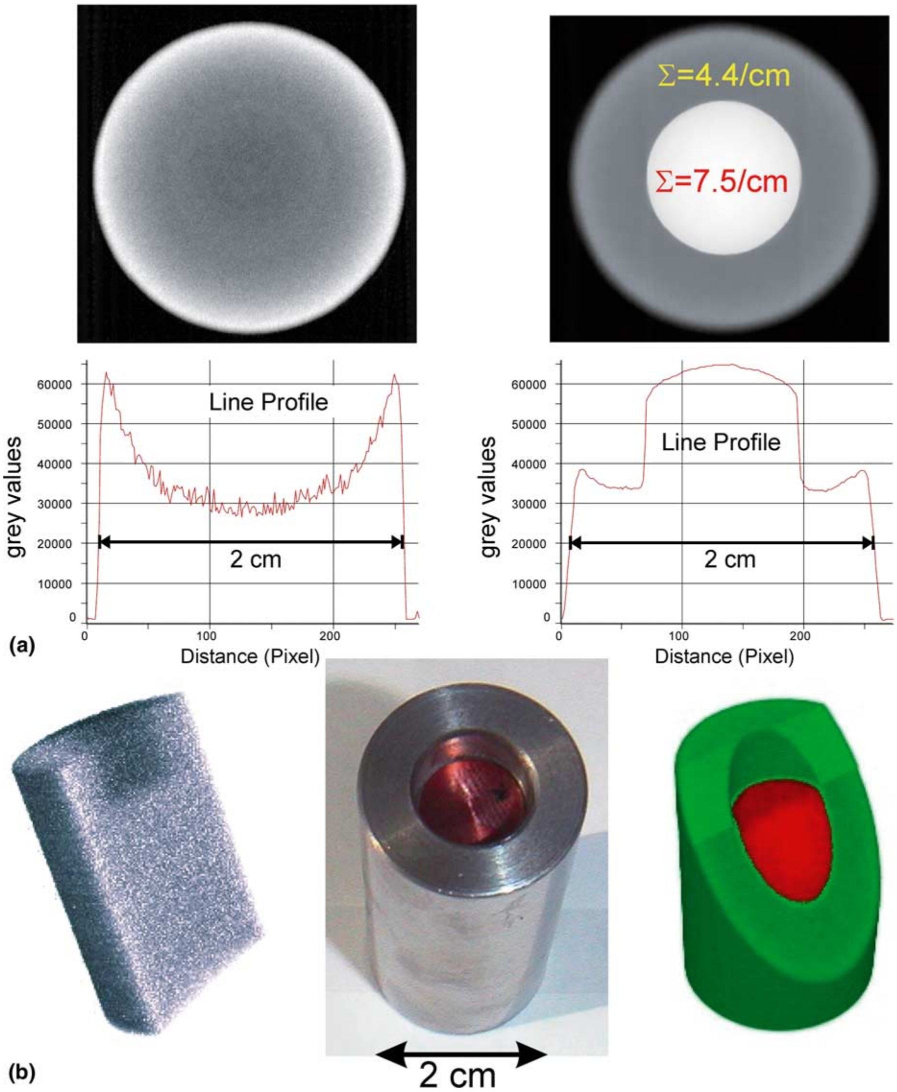

Fig. 4. Tomographic reconstruction and 3D rendering of a boron alloyed steel composite. (a) The ring has an outside diameter of 2 cm and a total macroscopic cross-section of $\Sigma_{t,\text{th}} = 4.4\ \text{cm}^{-1}$. The central rod contains higher boron content ($\Sigma_{t,\text{th}} = 7.5\ \text{cm}^{-1}$, $\varnothing = 1$ cm). Left: filtered backprojection from 60 projections. Right: filtered backprojection with beam hardening correction, (b) 3D rendering of 200 slices. Left: filtered backprojection without beam hardening correction. Middle: photograph of the steel composite. Right: rendering after beam hardening correction.

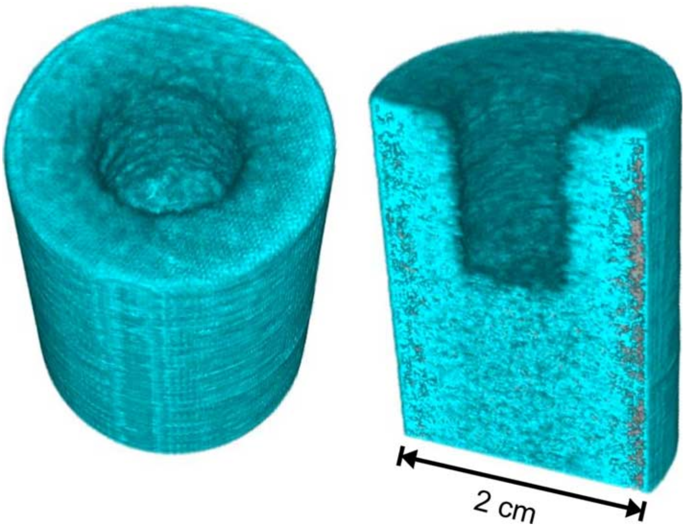

Fig. 5. ML reconstruction from only 10 projections of the same steel composite, shown in Fig. 4. The result is more satisfactory and less noisy than the FB reconstruction from 60 projections (Fig. 4, left). But without beam hardening correction the central rod with higher ^{10}B content cannot be extracted from the surrounding steel.

beam hardening correction is implemented in our ML routine.

Hitherto, we applied the tomographic technique primarily to our steel samples, but the macroscopic cross-section of uranium fuel elements lies within the range of the absorbing steels. The presented tomographic reconstruction algorithms can therefore also be employed in the non-destructive inspection of fuel elements, and it can be realized with rather weak neutron sources.

5. Summary

It has been demonstrated that tomographic investigations of strong absorbing materials are useful and feasible even with small reactor sources. From one tomographic set of projection data the variations of the effective and the thermal macroscopic cross-sections can be derived. Beam hardening artifacts have been removed by employing an exponential correction factor. Such a correction facilitates the quantitative analysis of the absorber distribution in case of polyenergetic neutron beams. Finally, we developed a maximum-likelihood algorithm, which considerably improves the tomographic reconstruction in the limit of few projections and fluctuating data. The presented techniques have been optimized within the framework of our steel project, but the methods can be adapted to other tomographic investigations where strong absorbing materials are involved.

Acknowledgements

The authors are grateful for the collaboration with BÖHLER Bleche GmbH, Mürzzuschlag in Austria, the financial support from the Austrian Science Foundation (Project No. P14229-PHY), and the Czech Ministry of Education (Project No. LN00A015).

References

[1] M. Zawisky, M. Bastürk, R. Derntl, F. Dubus, E. Lehmann, P. Vontobel, Appl. Radiat. Isotopes, in press.

[2] Böhler Bleche GmbH, Mürzzuschlag, Austria, Report on NEUTRONIT steel sheets, 1997.

[3] V.F. Sears, Neutron News 3 (3) (1992) 26.

[4] G.T. Herman, Image Reconstruction from Projections, Academic Press, London, 1980.

[5] A.C. Kak, M. Slaney, Computerized Tomographic Imaging, IEEE Press, 1987.

[6] M. Rivers, Tutorial Introduction to X-ray Computed Microtomography, 1998, www-fp.mcs.anl.gov/xray-cmt/rivers/.

[7] L.A. Shepp, B.F. Logan, IEEE Trans. Nucl. Sci. NS-21 (1974) 21.

[8] L.A. Shepp, Y. Vardi, IEEE Trans. Med. Imaging MI-1 (2) (1982) 113.

[9] J. Rehacek, Z. Hradil, M. Zawisky, W. Treimer, M. Strobl, Europhys. Lett. 59 (2002) 694.